Catalysis Science & Technology

ROYAL SOCIETY OF CHEMISTRY

MINI REVIEW

Cite this: *Catal. Sci. Technol.*, 2020, **10**, 2711

Integrated design for electrocatalytic carbon dioxide reduction

Xin Zhao,[a] Lijie Du,[b] Bo You *[b] and Yujie Sun *[c]

The electrocatalytic carbon dioxide reduction reaction (CO_2RR) to produce valuable fuels and chemicals with renewable energy inputs is an attractive route to convert intermittent green energy sources (*e.g.*, solar and wind) to chemical energy, alleviate our dependence on fossil fuels, and simultaneously reduce net carbon dioxide emission. However, the generation of reduced multi-carbon products with high energy density and wide applicability from the CO_2RR, such as oxygenates and hydrocarbons, suffers from high overpotential, slow reaction rate, and low selectivity due to its intrinsic multi-electron transfer nature. Moreover, the involved anodic oxygen evolution reaction (OER) also requires large overpotential and its product O_2 bears limited economic value. The potentially generated reactive oxygen species (ROS) during the OER may also degrade the membrane of a CO_2 reduction electrolyzer. Herein, we review the recent progress in novel integrated strategies to address the aforementioned challenges in the electrocatalytic CO_2RR. These innovative strategies include (1) concurrent CO_2 electroreduction *via* co-feeding additional chemicals besides CO_2 gas, (2) tandem CO_2 electroreduction utilizing other catalysts for converting the *in situ* formed products from the CO_2RR into more valuable chemicals, and (3) hybrid CO_2 electroreduction through integrating thermodynamically more favourable organic upgrading reactions to replace the anodic OER. We specifically highlight these novel integrated electrolyzer designs instead of focusing on nanostructured engineering of various electrocatalysts, in the hope of inspiring others to approach CO_2 electroreduction from a holistic perspective. The current challenges and future opportunities of electrocatalytic CO_2 reduction will also be discussed at the end.

Received 6th March 2020,
Accepted 7th April 2020

DOI: 10.1039/d0cy00453g

rsc.li/catalysis

1. Introduction

The development of the human society and the increasing worldwide population require massive energy, which is presently derived from non-renewable fossil fuels such as coal, oil, and natural gas since the Industrial Revolution.[1–3] However, excessive CO_2 emission from the utilization of fossil energy poses severely detrimental effects on the environment, climate and health of our planet, such as the greenhouse effect.[4–8] It necessitates intense research on sustainable CO_2 capture and conversion technologies.[6,7] In response, the renewable energy-driven room-temperature electrocatalytic CO_2 reduction reaction (CO_2RR) represents a viable alternative to utilize intermittent green energy sources (*e.g.*, sun and wind) for the conversion of otherwise waste CO_2 to chemical energy in the form of fuels and feedstocks like CO, methanol, ethylene, propanol and others (Fig. 1), which not only reduces our dependence on legacy fossil fuels but also mitigates the climatic deterioration.[8]

However, due to the extremely strong chemical bond in CO_2 (C═O, 806 kJ mol^{-1}),[9] the electrochemical CO_2RR usually needs large overpotentials to promote the sluggish kinetics, even highly active electrocatalysts are employed, which lower the energy conversion efficiencies.[4–9] Moreover, the most oxidized form of carbon in CO_2 renders the CO_2RR a multi-electron transfer nature and various products can be obtained through different pathways (Fig. 2), resulting in the low selectivity of the CO_2RR for a specific product.[4–9] Although many nanostructured materials such as single-atom catalysts,[9,10] noble-metal nanocrystals[11] and metal

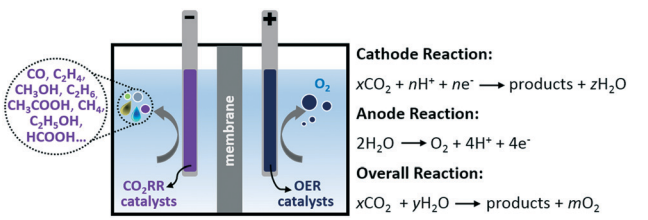

Fig. 1 Illustration of a traditional CO_2 reduction electrolyzer.

[a] *School of Science, Wuhan University of Technology, Wuhan, Hubei 430070, China*
[b] *Key Laboratory of Material Chemistry for Energy Conversion and Storage, Ministry of Education, School of Chemistry and Chemical Engineering, Huazhong University of Science and Technology, Wuhan, Hubei 430074, China. E-mail: youbo@hust.edu.cn*
[c] *Department of Chemistry, University of Cincinnati, Cincinnati, Ohio 45221, USA. E-mail: yujie.sun@uc.edu*

Reaction	E^0 (V vs RHE)	Product Name
$CO_2 + 2H^+ + 2e^- \rightarrow CO_{(g)} + H_2O$	−0.10	carbon monoxide
$CO_2 + 2H^+ + 2e^- \rightarrow HCOOH_{(aq)}$	−0.12	formic acid
$CO_2 + 6H^+ + 6e^- \rightarrow CH_3OH_{(aq)} + H_2O$	0.03	methanol
$CO_2 + 8H^+ + 8e^- \rightarrow CH_{4(g)} + 2H_2O$	0.17	methane
$CO_2 + 4H^+ + 4e^- \rightarrow C_{(s)} + 2H_2O$	0.21	graphite
$2CO_2 + 2H^+ + 2e^- \rightarrow (COOH)_{2(s)}$	−0.47	oxalic acid
$2CO_2 + 8H^+ + 8e^- \rightarrow CH_3COOH_{(aq)} + 2H_2O$	0.11	acetic acid
$2CO_2 + 10H^+ + 10e^- \rightarrow CH_3CHO_{(aq)} + 3H_2O$	0.06	acetaldehyde
$2CO_2 + 12H^+ + 12e^- \rightarrow C_2H_5OH_{(aq)} + 3H_2O$	0.09	ethanol
$2CO_2 + 12H^+ + 12e^- \rightarrow C_2H_{4(g)} + 4H_2O$	0.08	ethylene
$2CO_2 + 14H^+ + 14e^- \rightarrow C_2H_{6(g)} + 4H_2O$	0.14	ethane
$3CO_2 + 16H^+ + 16e^- \rightarrow C_2H_5CHO_{(aq)} + 5H_2O$	0.09	propionaldehyde
$3CO_2 + 18H^+ + 18e^- \rightarrow C_3H_7OH_{(aq)} + 5H_2O$	0.10	propanol

Fig. 2 Electrochemical CO_2 reduction reactions with equilibrium potentials. All of the standard potentials here are calculated *via* the Gibbs free energy of each reaction. CO_2 is always considered as a gas and water as a liquid.

complexes[12] have been reported to reduce CO_2 to CO with extremely high efficiency, the generation of more reduced multi-carbon products with higher energy density and wider applicability such as oxygenates and hydrocarbons is still limited by the low selectivity, slow production rate and few catalyst candidates, plus low energy conversion efficiency.[8] For example, Cu is generally considered to be the only metal that can form deeply reduced products with acceptable yields.[4b,5a,8] Currently, the well-designed reaction interface of a Cu catalyst reported by Sargent's group can reduce CO_2 to ethylene with a faradaic efficiency of 70% in an alkaline electrolyte (KOH) at an overpotential of 550 mV.[13] Another well-known limitation is the four-electron process of the involved oxygen evolution reaction (OER) at the anode during the CO_2RR, which also requires high overpotentials to complete the overall process and thus lowers the efficiency of the CO_2RR.[1b,3c,14] Furthermore, the OER product O_2 is not highly valuable and its side-products, reactive oxygen species (ROS), may degrade the electrolyzer membrane, resulting in premature failure of an electrolyzer.[1b] Overall, the practical cell voltage of the CO_2RR is always substantially larger than its thermodynamic potential.

To tackle the aforementioned challenges, most efforts have focused on engineering the electrocatalysts with varying facets, compositions, and defects, tailoring the reaction interface, and designing the membrane electrode assembly, as shown in recent excellent review papers.[5b,15–20] However, the recently developed integrated strategies for the system engineering of a CO_2RR electrolyzer have rarely been summarized, in spite of their promising role in practical CO_2 electroreduction. In this minireview, we present the recent progress in novel integrated strategies (Fig. 3) termed (1) concurrent CO_2 electroreduction *via* simultaneously feeding additional chemicals with CO_2 gas, (2) tandem CO_2 electroreduction utilizing other catalysts to convert the *in situ* formed products from the CO_2RR into more valuable chemicals, and (3) hybrid CO_2 electroreduction through integrating thermodynamically more favourable organic oxidation reactions to replace the anodic OER. For each type of integration, we summarize the major achievements and discuss the predominant trends for improving their performance. Finally, we provide our own perspective on the development of future integrated CO_2RR.

2. Integrated design for CO_2 electroreduction

2.1 Concurrent CO_2 electroreduction

Since CO_2 or CO only contains one carbon atom, coupling of two adsorbed CO intermediates during the CO_2RR and CORR is highly desirable and has been proposed as the rate limiting step for the generation of multi-carbon oxygenates and hydrocarbons.[4–8] Changing the coverage of adsorbed CO intermediates can dramatically vary the reaction pathways and hence the final products in terms of selectivities and yields.[4] In addition, the industrial waste streams are usually CO_2/CO mixtures.[21] It's thus technically and scientifically important to explore the electrocatalytic concurrent reduction of mixed CO_2/CO feeds (Fig. 3a). Accordingly, Strasser's group systematically studied the hydrocarbon generation rates on copper oxide nanoparticle (CuO_x NP) electrocatalysts under various CO_2/CO co-feeding conditions.[21] They found the significantly beneficial effect of mixed CO_2/CO co-feeds on

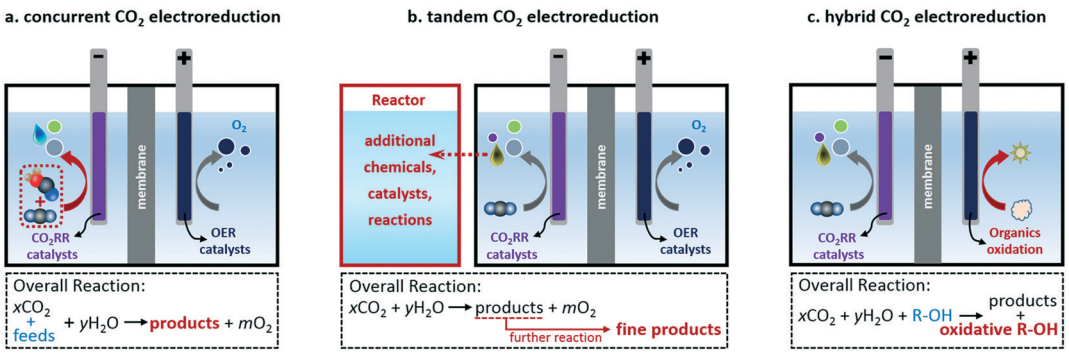

Fig. 3 Three innovative strategies: (a) concurrent CO_2 electroreduction, (b) tandem CO_2 electroreduction, and (c) hybrid CO_2 electroreduction for nonconventional CO_2RR.

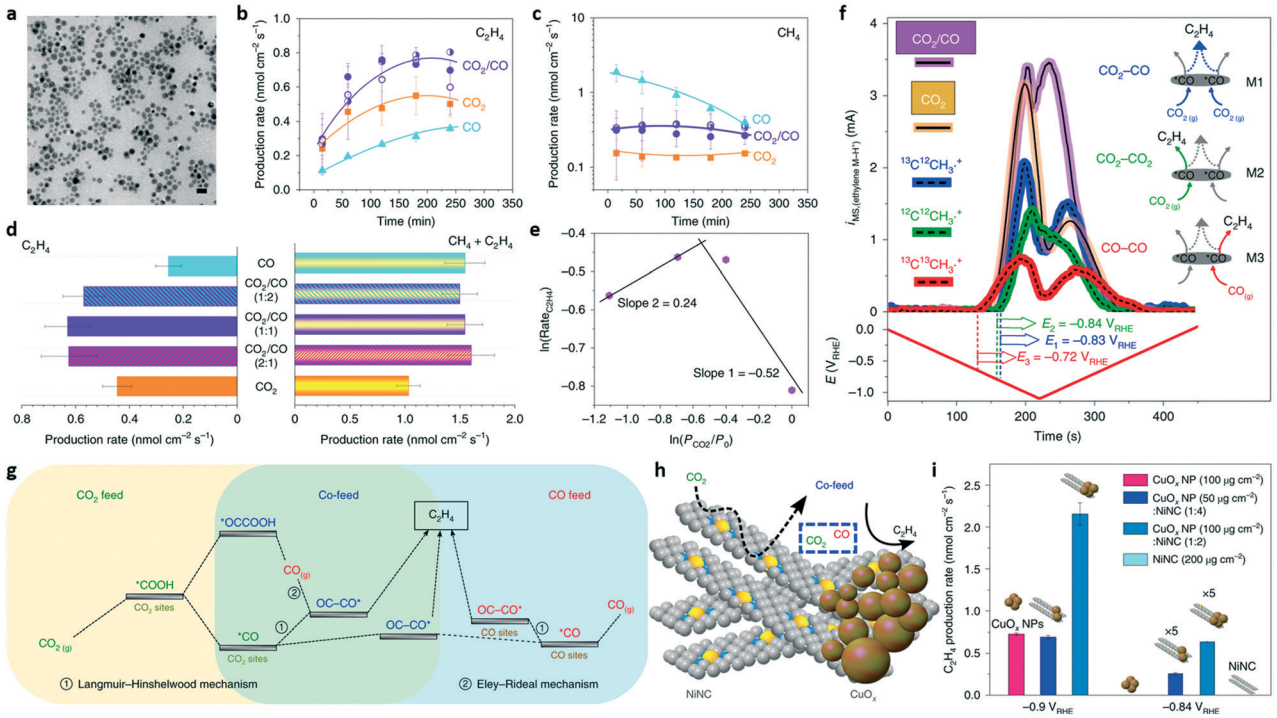

Fig. 4 (a) TEM image of CuO_x NPs. Scale bar, 20 nm. (b and c) Time-dependent absolute product formation rates for C_2H_4 (b) and CH_4 (c) at approximately −1.0 V *vs.* RHE. Orange, CO_2RR in CO_2-saturated 0.1 M $KHCO_3$ (pH = 6.8); cyan, CO_2RR in 0.1 M K_2HPO_4/KH_2PO_4 (pH = 6.9); purple, co-feed (CO_2/CO) reduction reactions in CO_2-saturated 0.1 M $KHCO_3$ for CO_2-to-CO partial pressure ratios of 2 : 1 (half-filled symbols), 1 : 1 (full-filled symbols), and 1 : 2 (empty symbols). (d) C_2H_4 production rates (left) and hydrocarbon production rates (CH_4 + C_2H_4) (right) with various ratios of feed-gas after 4 h. (e) $\ln(P_{CO_2}/P_0)$ *vs.* $\ln(\text{Rate}_{C_2H_4})$. P_{CO_2} is the partial pressure of CO_2, P_0 is 1 atm at 25 °C, and $\text{Rate}_{C_2H_4}$ is the average absolute product formation rate of C_2H_4. (f) Comparison of DEMS ion current sweeps over time for ethylene-related molecular fragments ($M–H^+$), fragments in the $^{12}CO_2/^{12}CO$ (1 : 3) co-feed (light purple curve) and the corresponding $^{12}CO_2$/Ar (1 : 3) feed (light-orange curve). A CO_2 partial pressure of 25 kPa and an Ar/CO partial pressure of 75 kPa were maintained in both cases. The bottom plot shows the concurrent cyclic voltammetric sweep over time. The deconvoluted DEMS ion current sweeps over time for the three possible $M–H^+$ ethylene fragments resulting from the isotope-labelled $^{12}CO_2/^{13}CO$ co-feed are shown by the blue, green, and red sweep profiles. The blue curve ($^{13}C^{12}CH_3^+$) represents the mechanistic pathway involving dimerization of one ^{13}CO-derived and one $^{12}CO_2$-derived *CO (cross coupling), shown in scheme M1. The green curve ($^{12}C^{12}CH_3^+$) represents the mechanistic pathway involving dimerization of two $^{12}CO_2$-derived *CO, shown in scheme M2. The red curve ($^{13}C^{13}CH_3^+$) represents the mechanistic pathway involving dimerization of two ^{13}CO-derived *CO, shown in scheme M3. The values of the onset potential ($E_{mechanism}$) referenced to the RHE are listed for each mechanism. (g) The demonstration of possible dimerization pathways with common intermediates in the CO_2 feed, co-feed and CO feed. (h) The tandem catalyst design combines a NiNC material, as a local CO-producer, and CuO_x NPs on a carbon-paper electrode. Grey, C atom; blue, N atom; yellow, Ni atom. (i) C_2H_4 production rate with the bifunctional hybrid catalyst for CO_2RR at various component concentrations and fixed overpotentials. Reproduced from ref. 21 with permission from Springer Nature, Copyright 2019.

the ethylene (C_2H_4) yield. The spherical CuO_x NPs were used as model electrocatalysts. Transmission electron microscopy (TEM) investigation revealed the monodispersity of CuO_x NPs with an average diameter of 9.4 ± 1.1 nm (Fig. 4a). Deconvolution of the Rietveld refined high-energy X-ray diffraction (HE-XRD) pattern of CuO_x NPs disclosed the co-presence of face-centred cubic Cu (18.0 ± 2.9 wt%), cubic Cu_2O (33.4 ± 5.3 wt%), and monoclinic CuO (39.2 ± 6.2 wt%). The electrocatalytic behaviours of these CuO_x NPs in pure CO_2, pure CO, and CO_2/CO mixtures (CO_x) were evaluated in neutral buffers with a two-compartment configuration. Potentiostatic electrolysis at −1.0 V *versus* the reversible hydrogen electrode (RHE) for several hours was used to assess the electrochemical CO_x reduction rates and the relevant selectivity. Fig. 4b and c showed the time-dependent absolute production rates of ethylene (C_2H_4) and methane (CH_4). It can be seen that the production rate of C_2H_4 is significantly promoted in the feeds of CO_2/CO mixtures over the entire range of feed ratios (Fig. 4b and d) compared to those in pure CO_2 and pure CO feeds. In contrast, the formation rate of CH_4 is strongly dependent on the feed compositions and follow the order CO > CO_2/CO > CO_2 (Fig. 4c). Considering the direct dependence of CH_4 formation on the redox state of a reactant, it's reasonable that the six-electron CO-to-CH_4 cascade reaction proceeds faster than the eight-electron pathway (CO_2-to-CH_4). Interestingly, by increasing the CO ratio in the co-feeds, the total production rate of both CH_4 and C_2H_4 (simply called the hydrocarbon production rate) sharply increased by about 50% (Fig. 4d right), despite a lower concentration of total CO_x in electrolyte. Given the fact that pure CO favours proton accessibility to adsorbed intermediates, it was concluded that a hydrogenated dimer (*CO–COH) generated in a consecutive electron–proton McMurry coupling-type transfer accounted

for the C_2H_4 formation,[22] different from the reaction mechanism of the CH_4 generation. The non-monotonic relationship between the C_2H_4 production rate and CO_2 partial pressure (Fig. 4e) hindered an optimum CO_2-to-CO ratio featuring the maximum C_2H_4 yields.

To understand the enhanced mechanism of C_2H_4 production in co-feeds, an *operando* differential electrochemical mass spectrometer (DEMS) equipped with a newly designed capillary cell with millisecond time resolution was developed and employed to track and quantify the origins of two individual carbon atoms in the produced C_2H_4 *via* ^{13}CO isotope-labelling. The ion mass currents of hydrogen-abstracted molecular fragments ($M–H^+$) represented real-time C_2H_4 products under cathodic and anodic scan directions (Fig. 4f). In the cathodic scanning region, the ion mass current for C_2H_4 production with the $^{12}CO_2/^{12}CO$ co-feed (purple curve in Fig. 4f) almost overlapped with that with the $^{12}CO_2$ feed (orange curve in Fig. 4f), implying that the dimerization of CO_2-derived surface-adsorbed *CO accounts for the C_2H_4 formation and this self-feeding of CO from CO_2 reduction was seemingly sufficient. Meanwhile in the anodic scanning region, only the $^{12}CO_2/^{12}CO$ co-feed guaranteed the comparable generation of C_2H_4, suggesting the presence of CO depletion at the electrocatalytic interface. The isotope-labelled $^{12}CO_2/^{13}CO$ co-feed and $^{12}CO_2$/Ar and ^{13}CO/Ar feeds with comparable partial pressures were then investigated to deconvolute the origin of the carbon atoms in C_2H_4 and to assess the respective contributions of the three competing pathways for C_2H_4 formation (red, blue and green curves in Fig. 4f). The red curve corresponded to the $^{13}C_2H_3^+$ fragment of the $^{13}CO–^{13}CO$ pathway with a current of $I_{m/z=29}$, where CO stemmed entirely from the ^{13}CO feed; the green curve corresponded to the $^{12}C_2H_3^+$ fragment of the $^{12}CO–^{12}CO$ pathway with a current of $I_{m/z=27}$, where CO stemmed entirely from the non-labelled CO_2 feed; and the blue curve corresponded to the $^{13}C^{12}CH_3^+$ fragment ($I_{m/z=28}$) related to the $^{12}CO_2–^{13}CO$ coupling pathway, where ethylene was formed from CO originating from CO_2 and from ^{13}CO in the feed. The respective three CO dimerization pathways to C_2H_4 are schematically illustrated using their corresponding colours (M1–M3). This DEMS analysis also demonstrated that the onset potential (E) for C_2H_4 production positively shifted by about 120 mV in the pure CO feed (E_{CO} = −0.72 V_{RHE}) compared to that in the pure CO_2 feed (E_{CO_2} = −0.84 V_{RHE}), suggesting the faster kinetics of the electrocatalytic CO reduction to C_2H_4. Deep analysis and integration of the three curves uncovered that 67% of C_2H_4 could be attributed to CO in the feed during the CO_xRR. On the basis of the above results, the authors sketched the reaction mechanisms under the three feed conditions, as shown in Fig. 4g. Two types of two-site hypotheses including Langmuir–Hinshelwood and Eley–Rideal (ER)-type reaction pathways were proposed. To mimic the co-feed conditions, the authors prepared a bifunctional tandem catalyst containing NiNC of high surface area as a CO producer and a support and CuO_x NPs as dimerization sites for C_2H_4 production (Fig. 4h). As shown in Fig. 4i, the electrocatalytic performance of the CuO_x–NiNC tandem catalyst for C_2H_4 generation from the CO_2RR was largely enhanced compared to pure CuO_x NPs at two applied potentials. Moreover, the CuO_x–NiNC tandem catalyst produced less free CO gas at an overpotential of −0.84 V_{RHE} relative to pure NiNC, suggesting that some of the generated CO on NiNC was immediately consumed by CuO_x in the tandem catalyst.

Koper's group reported the co-reduction of CO_2 with the addition of methanol to produce dimethyl carbonate.[23] By using *in situ* Fourier transform infrared (FTIR) spectroscopy, the authors showed the formation of an intermediate containing C═O and C–O groups from the reaction between methoxy groups from methanol with generated CO from the CO_2RR on diverse catalysts such as Cu, Pt and Pb. More recently, Xu's group fed acetaldehyde during the CORR on oxide-derived copper (OD-Cu) and found that 36% of 1-propanol can be produced from the coupling of an adsorbed methylcarbonyl intermediate from acetaldehyde and CO.[24]

Besides promising C–C coupling to multi-carbon feedstocks, Jiao's group recently demonstrated that C–N bonds could be formed through NH_3 feeding during a CO_2-derived CORR on highly crystalline Cu NPs with a small fraction of Cu oxides.[25] The overall strategy is schematically outlined in Fig. 5a. Under steady-state galvanostatic electrolysis in 1 M KOH, a total current density of 500 mA cm^{-2} was observed for approximately 80% C_{2+} products including ethylene, ethanol, acetate, and *n*-propanol (Fig. 5b left). After feeding NH_3 gas with CO in a molar ratio of 2 : 1 (NH_3 : CO), the applied potential increased by ~30 mV to afford the same current density probably due to the reduced CO partial pressure. However, the addition of NH_3 considerably increased the acetamide yield with a faradaic efficiency of up to 38% and a current density of 114 mA cm^{-2} at −0.68 V *vs.* RHE (Fig. 5b right). Meanwhile, the faradaic efficiencies for the formation of both ethylene and alcohols decreased at moderate to high overpotentials, whereas that for acetate was almost unchanged. Instead of NH_3, ammonium hydroxide led to similar results, suggesting that acetamide could be produced in both gas and liquid NH_3. Increasing the KOH concentration shifted the selectivity from amide to acetate during the CORR, implying that a ketene intermediate was probably formed and nucleophilically attacked by either OH^- or NH_3 to form acetate or acetamide, respectively (Fig. 5c). Because the ketene intermediate contained only one oxygen from CO, another oxygen in the resulting acetate should originate from water. A ^{18}CO isotopic labelling study verified that the oxygen in acetamide came from CO, further evidencing the proposed ketene-mediated reaction mechanism (Fig. 5c). Full-solvent quantum mechanical calculations showed that two CO molecules dimerized followed by sequential H transfer from two surface water molecules to form the *(HO)C═COH intermediate, which then went through two different pathways. One formed *C═COH which accounts for ethylene (65%) and ethanol/*n*-

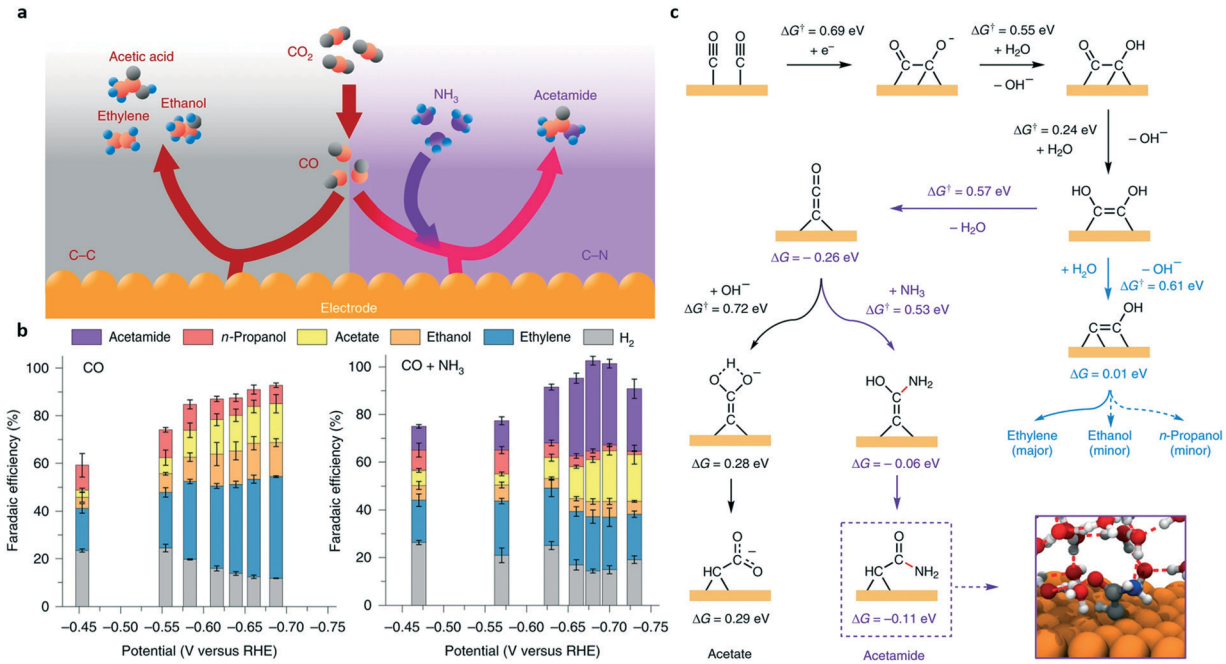

Fig. 5 (a) Scheme of NH_3 induced C–N bond formation during CO_2-derived CORR. (b) Faradaic efficiencies *vs.* the applied potential for the reduction of CO (left) and CO + NH_3 (right). (c) Mechanism of CO_2-derived CORR on Cu that shows how it splits at [*(HO)C═COH] into two pathways. Reproduced from ref. 25 with permission from Springer Nature, Copyright 2019.

propanol (35%). The other led to the formation of *C═C═O through a water-mediated pathway, which is attacked by either OH^- or NH_3 to form acetate or acetamide, respectively (Fig. 5c). With these insights, Jiao *et al.* extended the reaction substrate to methylamine, ethylamine and dimethylamine, and results analogous to the CO/NH_3 co-feeding were obtained where substantial amounts of *N*-methylacetamide, *N*-ethylacetamide and *N*,*N*-dimethylacetamide were produced at total current densities of up to 300 mA cm^{-2} with maximum faradaic efficiencies of 42%, 34%, and 36%, respectively. The ability to generate heteroatom-containing carbon species would increase the potential of CO_2 or CO electrolysis technologies for practical applications.

2.2 Tandem CO_2 electroreduction

Despite the substantial progress that has been made to improve the activity and selectivity to C_1, C_2 and even C_3 products with appreciable efficiencies, the direct and highly selective CO_2RR to C_{3+} products still remains a major challenge.[26–28] A promising strategy to address this concern is to directly transform the products from the CO_2RR *via* biological catalysts (*i.e.*, bacterium), as so-called "tandem CO_2 electroreduction" (Fig. 3b).

For example, Schmid's group described the highly efficient production of butanol and hexanol from CO_2 and H_2O with renewable energy, which was achieved by solar-powered CO_2RR in tandem with a bioprocess module (fermentation) for anaerobic conversion of the products of the CO_2RR (Fig. 6a).[26] For the CO_2 electrolyzer, an Ag-based gas diffusion electrode served as the cathode to afford high current density and IrO_x as the anode. Not all the CO_2 feed was converted to CO and H_2 was co-formed due to proton reduction. The total faradaic efficiencies of CO and H_2 were around 100% (Fig. 6b), suggesting the absence of other gases like O_2. For instance, at a current density of 300 mA cm^{-2} and a CO_2 flow rate of 90 sccm (standard cubic centimetre per min), the faradaic efficiencies of CO and H_2 were nearly 70% and 30%, respectively (Fig. 6b), and both remained almost constant for more than 1200 h (Fig. 6c). The absence of O_2 in the outlet syngas (CO and H_2, and CO_2) was vital for the following bioprocess module, because high O_2 concentration is toxic for the bacteria in the fermentation phase.

Given the excellent performance of the well-developed CO_2 electrolyzer, the authors firstly coupled it with a commercially available photovoltaic (PV) device and syngas was produced at a rate of 16.52 sccm with a composition of 11.76% CO (4.8 mmol h^{-1}), 6.37% H_2 (2.6 mmol h^{-1}) and 81.86% CO_2 (33.4 mmol h^{-1}). For the conversion to high-value acetate and ethanol (Fig. 6d), the resulting mixture was then fed with 1 L fermenters with *C. autoethanogenum* acetogen and 0.5 L culture at 36 °C.[26,29] Stationary conditions were reached after 50 h, where the cell concentration, the consumption rates of CO and H_2, and the production rates of acetate and ethanol were constant for the next 45 h. The consumption of CO and H_2 syngas (3.35 mmol h^{-1}) agreed well with the reduction of CO_2 to acetate and ethanol, suggesting a faradaic efficiency of almost 100% (Fig. 6e). Based on the ethanol production, the calculated efficiency of energy conversion (EE) in this

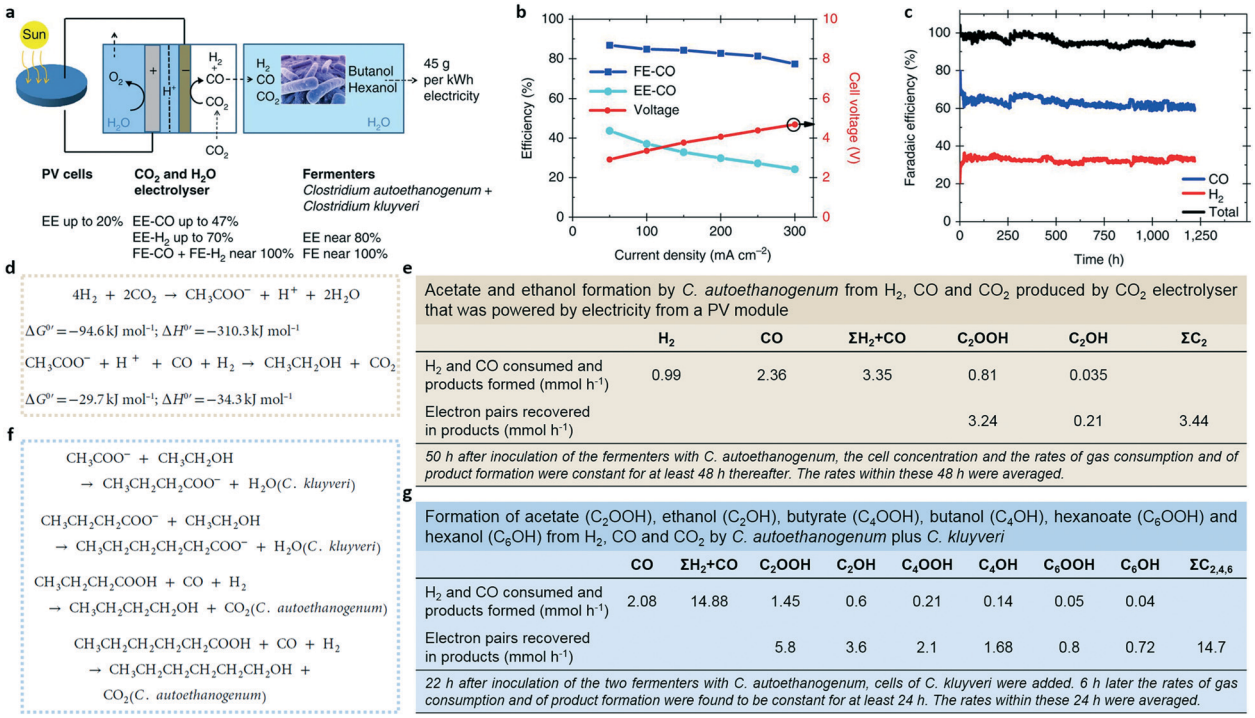

e

Acetate and ethanol formation by *C. autoethanogenum* from H_2, CO and CO_2 produced by CO_2 electrolyser that was powered by electricity from a PV module

	H_2	CO	ΣH_2+CO	C_2OOH	C_2OH	ΣC_2
H_2 and CO consumed and products formed (mmol h^{-1})	0.99	2.36	3.35	0.81	0.035	
Electron pairs recovered in products (mmol h^{-1})				3.24	0.21	3.44

50 h after inoculation of the fermenters with C. autoethanogenum, the cell concentration and the rates of gas consumption and of product formation were constant for at least 48 h thereafter. The rates within these 48 h were averaged.

g

Formation of acetate (C_2OOH), ethanol (C_2OH), butyrate (C_4OOH), butanol (C_4OH), hexanoate (C_6OOH) and hexanol (C_6OH) from H_2, CO and CO_2 by *C. autoethanogenum* plus *C. kluyveri*

	CO	ΣH_2+CO	C_2OOH	C_2OH	C_4OOH	C_4OH	C_6OOH	C_6OH	$\Sigma C_{2,4,6}$
H_2 and CO consumed and products formed (mmol h^{-1})	2.08	14.88	1.45	0.6	0.21	0.14	0.05	0.04	
Electron pairs recovered in products (mmol h^{-1})			5.8	3.6	2.1	1.68	0.8	0.72	14.7

22 h after inoculation of the two fermenters with C. autoethanogenum, cells of C. kluyveri were added. 6 h later the rates of gas consumption and of product formation were found to be constant for at least 24 h. The rates within these 24 h were averaged.

Fig. 6 (a) Scheme of the tandem CO_2RR modules used in the synthesis of 1-butanol and 1-hexanol from CO_2 and H_2O. (b) Dependence of faradaic efficiencies (FEs) and energy conversion efficiencies (EEs) on the current densities. The anolyte and catholyte solutions, 0.1 M K_2SO_4/1.5 M $KHCO_3$ (pH ≈ 7), were continuously cycled and mixed at a flow rate of 200 ml min^{-1}. The temperature was 30 °C and the CO_2 flow rate was 90 sccm. (c) Stability of CO-FE and H_2-FE at an electric current density of 300 mA cm^{-2}. The cell voltage remained constant within 7.0–7.5 V during the course of the experiment. The cathode and anode were 9.5 mm apart and separated by a high-conductivity, zirconium-oxide-based diaphragm. The anolyte and catholyte solutions, 0.4 M K_2SO_4/0.5 M $KHCO_3$ (pH ≈ 7), were continuously cycled and mixed at a flow rate of 200 ml min^{-1}. The temperature was 30 °C and the CO_2 flow rate was 100 sccm. (d) Reactions and (e) data for acetate and ethanol formation by *C. autoethanogenum* from H_2, CO, and CO_2 produced using the CO_2 electrolyzer that was powered by electricity from a PV module. (f) Reactions and (g) data for the formation of acetate (C_2OOH), ethanol (C_2OH), butyrate (C_4OOH), butanol (C_4OH), hexanoate (C_6OOH), and hexanol (C_6OH) from H_2, CO, and CO_2 by *C. autoethanogenum* plus *C. kluyveri*. Reproduced from ref. 26 with permission from Springer Nature, Copyright 2018.

fermentation was about 80%. Considering the 50% EE for the CO_2 reduction electrolyzer at 50 mA cm^{-2} and 20% EE for the PV module, the overall EE was as high as 8%.

Further inoculating the above fermenters with *C. kluyveri* led to the conversion of acetate and ethanol to butyrate and hexanoate and then to butanol and hexanol (Fig. 6f). The authors then initiated the CO_2 electrolyzer at 150 mA cm^{-2} to constantly generate syngas with a flow rate of 16.23 sccm and a composition of 10% CO (4 mmol h^{-1}), 60% H_2 (24.2 mmol h^{-1}) and 30% CO_2 (12.2 mmol h^{-1}). Again the syngas was fed into 1 L fermenters with 0.5 L *C. autoethanogenum* culture for 22 h followed by additional inoculation with *C. kluyveri*. At the moment of addition, acetate and ethanol were already formed from CO, H_2 and CO_2 by *C. autoethanogenum* (Fig. 6d). The additional inoculation gave rise to the formation of butanol and hexanol by *C. autoethanogenum* and *C. kluyveri* (Fig. 6f). After approaching stationary state conditions, the rates of CO and H_2 consumption and those of acetate and ethanol formation remained constant for 45 h. The consumed amounts of CO and H_2 (14.88 mmol h^{-1} in total) again agreed well with the molar electron pairs (14.52 mmol h^{-1}) required to reduce CO_2 to the three acids and alcohols (Fig. 6g), indicating the high faradaic efficiency close to 100%. The EE for butanol and hexanol formation was calculated to be about 78% at a rate of 0.6×10^{-3} moles per hour per litre of culture. In addition to *C. kluyveri*, other microorganisms like *Pelobacter propionicus* can be combined with *C. autoethanogenum* to ferment ethanol and CO_2 to propionate and acetate or oleaginous yeast, and to convert ethanol and acetate to lipids. The superior flexibility of this tandem design leads to the production of various platform chemicals bearing high faradaic efficiencies.

Recently, Ager's group reported a two-step sequential electrocatalytic process to convert CO_2 into C_{2+} hydrocarbons and oxygenates by situating the Ag electrode upstream of the Cu electrode in a continuous flow reactor, at which CO was formed from CO_2 reduction on Ag, and further converted into C–C coupled products on Cu. By combining convection–diffusion simulations and electrochemical experiments, the optimal device led to a relative increase in the formation rate of C_2 and C_3 oxygenates as compared to ethylene.[30]

2.3 Hybrid CO_2 electroreduction

For a conventional CO_2 electrolyzer, the OER takes place to complete the electrocatalysis cycle, which requires large

overpotential to produce appreciable current density.[31–36] Thermodynamic analysis indicates that the OER leads to an energy loss of about 90% during CO_2 reduction to CO.[33] Also, its product O_2 is not highly valuable and the side products of the OER, reactive oxygen species, may degrade the electrolyzer membrane and hence shorten the durability of electrolyzers. Similar to hybrid water electrocatalysis,[1b,3c] replacing the OER with thermodynamically more favourable organic oxidative upgrading reactions would not only lower the voltage input and exclude the formation of ROS, but also produce more valuable organic products on the anode,[37–41] maximizing the energy return of CO_2 electroreduction (Fig. 3c).

Berlinguette's group reported the cathodic reduction of CO_2 to CO integrated with the anodic oxidation of four classes of representative alcohols to the corresponding carbonyl compounds (Fig. 7a) in a single two-compartment electrochemical cell.[32] Each compartment contained 25 mL of 0.5 M $NaHCO_3$ aqueous solution and was separated by a Nafion proton exchange membrane. A Cu–In alloy film on titanium served as the cathode and a platinum mesh was used as the anode. The polarization curve of the CO_2RR at the Cu–In cathode showed an onset potential of about −0.36 V *vs.* RHE and a current density of 3.7 mA cm^{-2} at −0.70 V *vs.* RHE (Fig. 7b) with a faradaic efficiency of 80% for the formation of CO. This high performance enabled a reliable platform for the study of hybrid electrolysis. Electrochemical oxidation of four alcohols was then investigated in the same electrolyte. As shown in Fig. 7c, 1-phenylethanol (1-PEA) was used as a substrate (the other three alcohols exhibited similar behaviour). Because Pt cannot directly oxidize 1-PEA, TEMPO was employed as a redox mediator. The cyclic voltammogram of TEMPO exhibited a reversible redox couple at 1.3 V *vs.* RHE. After adding 1-PEA, the current density increased slightly, indicative of charge transfer between TEMPO and 1-PEA and the more favourable alcohol oxidation than the OER in the potential window of 1.2–1.8 V *vs.* RHE. A two-electrode hybrid CO_2 electroreduction process was then conducted at a constant potential of −0.70 V for 3 h at which a stable current density of about 3.7 mA cm^{-2} was maintained (Fig. 7d). Quantitative analysis confirmed that the faradaic efficiencies were above 70% over the entire 3 h, while the faradaic efficiency for the oxidation of 1-PEA to acetophenone (ACP) was *ca.* 95% for the first 30 min and then decreased to approximately 70% at 1.5 h. The OER became dominant for the last 1.5 h due to the gradual consumption of 1-PEA (Fig. 7e), and thus the average faradaic efficiency for ACP formation was calculated to be merely 36% over the entire experiment. The other three alcohols were all oxidized with yields of 78–93% after 3 h electrolysis. These results collectively indicated that the formation of CO and ACP is favoured over the competing HER and OER until depletion of alcohol substrates, respectively, suggesting the success of the proposed hybrid CO_2 electroreduction.

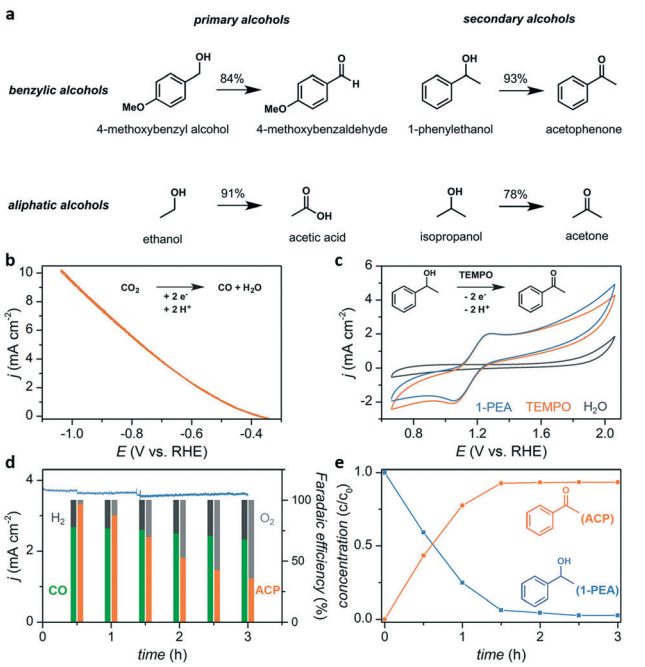

Fig. 7 (a) Reactions tested herein to demonstrate the oxidation of primary and secondary benzylic alcohols, as well as primary and secondary aliphatic alcohols. (b) Reductive scan of a Cu–In cathode at a rate of 5.0 sccm. (c) Cyclic voltammogram of a blank aqueous solution prior to the successive addition of 0.20 mmol TEMPO and 0.25 mmol 1-phenylethanol (1-PEA). (d) Rate of product formation (blue trace) and faradaic efficiencies (columns) over 3 h hybrid electrolysis at an external bias of −0.70 V that converts CO_2 into CO and 1-phenylethanol (1-PEA) into acetophenone (ACP). (e) Relative concentrations of 1-phenylethanol and acetophenone over the 3 h experiment. Reproduced from ref. 32.

More recently, Kenis's group replaced the OER with the oxidation of high-volume building block chemicals such as glycerol, a cheap by-product of industrial biodiesel and soap production and biomass-derived glucose.[33] From a combined theoretical and experimental approach, it was revealed that this process lowered the cell potential for CO_2 electroreduction by approximately 0.85 V, resulting in a reduction in the electricity consumption by up to 53%. From the thermodynamic point of view, the standard Gibbs free energies of the CO_2 reduction to CO and the OER are 20.1 and 237.1 kJ mol^{-1}, respectively, indicative of 92.2% of the overall energy consumption for driving the OER. Fig. 8 showed the calculated standard cell voltage ($|E^0_{cell}|$) for the combination of CO_2-to-CO reduction and the oxidation of glycerol or glucose. The results hinted that a noteworthy lowering of $|E^0_{cell}|$ and hence electricity requirements can be saved. To assess the practicality of the above proposed processes, they performed electrochemical evaluation of different hybrids using a gas diffusion layer (GDL) electrode-based flow electrolyzer. The catholyte was 2.0 M KOH, while the anolyte was a mixture of 2.0 M KOH and 2.0 M glycerol or a mixture of 2.0 M KOH and 2.0 M glucose for the electro-oxidation of glycerol and glucose, respectively. Fig. 8b demonstrated that coupling the electro-oxidation of glycerol or glucose rather than the OER on a Pt black-coated GDL anode reduced the onset cell potential for the reduction of

a

Cathode reaction	Possible anode reactions	Possible overall reactions	$\lvert E^0_{cell}\rvert$ (V)
$CO_2 \rightarrow CO$	Water → oxygen $2OH^- \rightarrow H_2O + 0.5O_2 + 2e^-$	$CO_2 \rightarrow CO + 0.5O_2$	1.33
	Glycerol → glyceraldehyde $C_3H_8O_3 + 2OH^- \rightarrow C_3H_6O_3 + 2H_2O + 2e^-$	$CO_2 + C_3H_8O_3 \rightarrow CO + C_3H_6O_3 + H_2O$	0.51
	Glycerol → lactic acid $C_3H_8O_3 + 2OH^- \rightarrow C_3H_6O_3 + 2H_2O + 2e^-$	$CO_2 + C_3H_8O_3 \rightarrow CO + C_3H_6O_3 + H_2O$	0.35
$CO_2 + H_2O + 2e^- \rightarrow CO + 2OH^-$	Glycerol → HCOOH $C_3H_8O_3 + 8OH^- \rightarrow 3HCOOH + 5H_2O + 8e^-$	$CO_2 + 0.25C_3H_8O_3 \rightarrow CO + 0.75HCOOH + 0.25H_2O$	0.24
	Glucose → gluconic acid $C_6H_{12}O_6 + 2OH^- \rightarrow C_6H_{12}O_7 + H_2O + 2e^-$	$CO_2 + C_6H_{12}O_6 \rightarrow CO + C_6H_{12}O_7$	0.03
	$CH_4 \rightarrow CH_3OH$ $CH_4 + 2OH^- \rightarrow CH_3OH + H_2O + 2e^-$	$CO_2 + CH_4 \rightarrow CO + CH_3OH$	0.73
	$CH_4 \rightarrow CO$ $CH_4 + 6OH^- \rightarrow 5H_2O + CO + 6e^-$	$0.75CO_2 + 0.25CH_4 \rightarrow CO + 0.5H_2O$	0.36

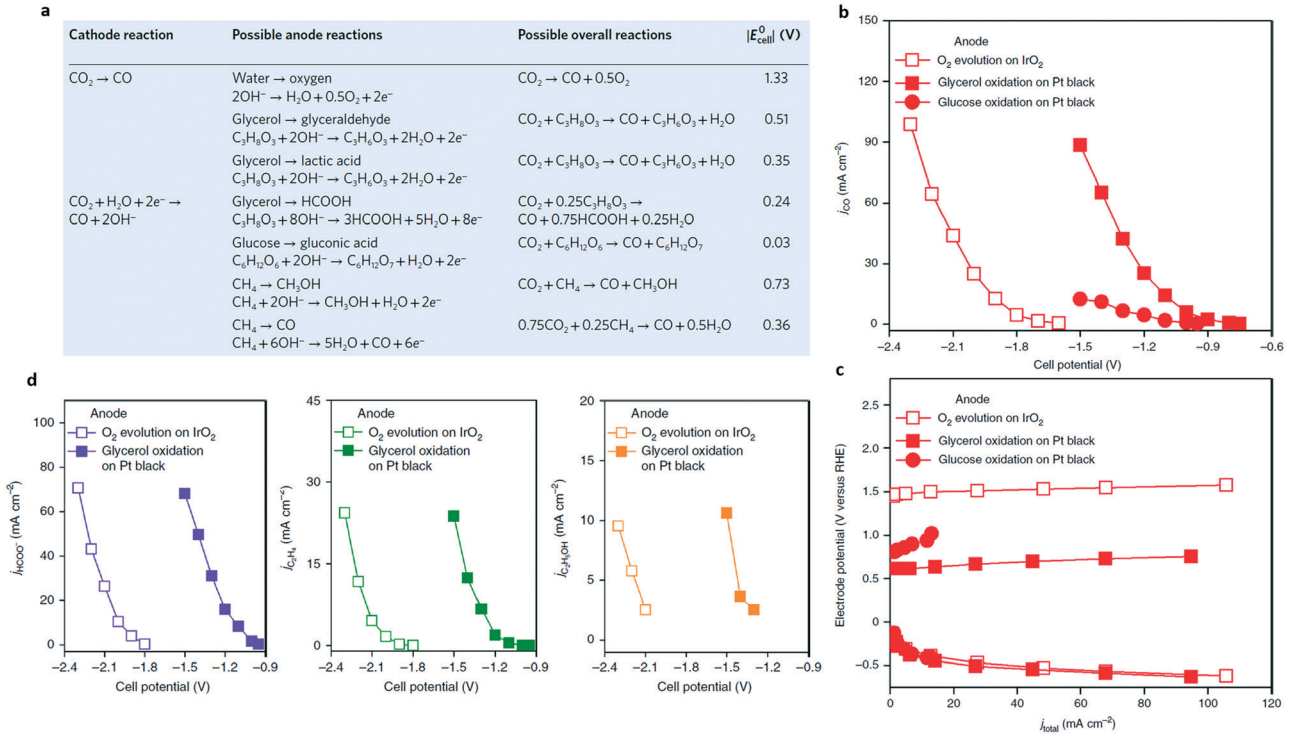

Fig. 8 (a) Theoretical $|E^0_{cell}|$ for the cathodic electroreduction of CO_2 to CO coupled with anodic OER or glycerol and glucose electro-oxidation. (b) Curves of current density of CO production *versus* cell potential for the cathodic electroreduction of CO_2 to CO on Ag coupled with anodic OER, glycerol oxidation, or glucose oxidation. (c) Individual electrode potential as a function of total current density. (d) Curves of current density of $HCOO^-$ production on Sn (left) and C_2H_4 (middle) and C_2H_5OH (right) production on Cu *versus* cell potential for cathodic electroreduction of CO_2 coupled with anodic glycerol oxidation. Reproduced from ref. 33 with permission from Springer Nature, Copyright 2019.

CO_2 to CO on an Ag-coated GDL cathode from −1.6 V to −0.75 and −0.95 V, respectively. Also, the partial current density of CO (j_{CO}) for the glycerol electro-oxidation was much higher than that for the glucose electro-oxidation, suggestive of the more promising effect of the former. Based on j_{CO}, electro-oxidation of glycerol instead of the OER resulted in a 37–53% reduction of electricity requirements and thus improved the process economics. A single-electrode plot suggested that the major improvement was ascribed to the anode while the cathodic CO_2 electroreduction was not affected (Fig. 8c). Product quantification confirmed the formation of value-added chemicals such as $HCOO^-$ and lactate from the glycerol electro-oxidation, which further improved the economics of the overall hybrid process. A similar decrease of onset cell potentials for the electroreduction of CO_2 to $HCOO^-$, C_2H_4, and C_2H_5OH was also observed when using the glycerol electro-oxidation instead of the OER (Fig. 8d). For example, the onset cell potentials for the electroreduction of CO_2 to $HCOO^-$ on a Sn-coated GDL cathode, and to C_2H_4 and C_2H_5OH on a Cu-coated GDL cathode decreased from −1.75, −1.8, and −2.1 V to −0.9, −0.95, and −1.3 V, respectively. Finally, durability tests indicated that the cell potential and faradaic efficiency for CO generation were stable over 1.5 h.

Apart from alcohol oxidation, dye oxidation removal is another alternative to replace the OER. Purkait's group used crystal violet oxidation on a non-precious metal Co_3O_4 anode to replace the OER.[42]

3. Conclusions

In this minireview, we have summarized the recent integrated strategies to address concerns in the electrocatalytic CO_2RR to multi-carbon products with higher energy density and wider applicability, including high overpotentials, low selectivity and slow reactivity. These innovative strategies include (1) concurrent CO_2 electroreduction *via* deliberately feeding additional gas or liquid chemicals besides CO_2 gas to favour the formation of high-value products, (2) tandem CO_2 electroreduction utilizing other catalysts to convert the *in situ* formed products from the CO_2RR into more valuable chemicals, and (3) hybrid CO_2 electroreduction through integrating thermodynamically more favourable organic upgrading reactions to replace the anodic OER for lower energy inputs. These strategies are different from the conventional focus of electrocatalyst design for high performance. Even though such new directions are still in an early stage, some pioneering studies demonstrate their promising role in the practical CO_2 electroreduction. Despite the tremendous progress that has been made, there still exist many challenges and opportunities in these fields.

In terms of concurrent CO_2 electroreduction, more substrates need to be explored for co-reduction with CO_2 or CO. For instance, Sargent's group recently reported that nitrate (NO_3^-) can be electrochemically reduced using Cu and

a CuNi alloy to NH_3 in 1.0 M KOH.[43] The relevant experimental parameters such as the Cu electrocatalysts and the pH of the electrolyte (1.0 M KOH) are the same as those for the CO_2RR or CORR, such that it's very promising to investigate the co-reduction of CO_2 or CO with NO_3^-. In addition, the underlying origin of improved selectivity under co-feed conditions is still not fully understood, and *in situ* spectroscopic studies combined with theoretical investigations should be systematically employed to provide deep insights.

For tandem CO_2 electroreduction, it's vital to optimize the process design due to the continuous conditions in an industrial process, which is different from that in laboratories. Matching the system components is a prerequisite for continuous operation to avoid the possible accumulation of intermediates.

Besides exploring more abundant organics such as biomass and biowaste for hybrid CO_2 electroreduction, a key fact is that although many organic oxidation processes are much easier than oxygen evolution, the required overpotentials are still quite high given the relatively low thermodynamic potentials of these organic oxidation reactions. In some cases, the issue of electrocatalyst poisoning by organics could be severe. It's thus challenging to explore highly efficient, robust and low-cost anodic electrocatalysts for this hybrid electrocatalysis strategy. Structure engineering is effective in tuning the local solid–liquid interfaces of electrocatalysts and thus modulates their electrochemical performance, such as shaping, doping and strain creating.[44]

In addition to the development of the introduced strategies, much higher integration and diverse coupling are desirable as well to further improve the economics of the CO_2RR. For example, although both concurrent CO_2 electroreduction and tandem CO_2 electroreduction strategies can enhance the generation of multi-carbon products, the OER is still involved in their anodes. Incorporation of tandem and hybrid CO_2 electroreduction is expected to further improve the overall energy conversion efficiency and return of the integrated devices. Finally, careful technoeconomic analysis should be conducted before commercialization.

Conflicts of interest

There are no conflicts to declare.

Acknowledgements

Y. S. acknowledges the financial support from the Herman Frasch Foundation (820-HF17), the National Science Foundation (CHE-1914546), and the University of Cincinnati. B. Y. acknowledges the financial support from the Start-up Funding of the Huazhong University of Science and Technology (HUST) and the Program for HUST Academic Frontier Youth Team.

Notes and references

1 (*a*) S. Chu, Y. Cui and N. Liu, *Nat. Mater.*, 2017, **16**, 16; (*b*) B. You and Y. Sun, *Acc. Chem. Res.*, 2018, **51**, 1571.

2 (*a*) B. M. Hunter, H. B. Gray and A. M. Müller, *Chem. Rev.*, 2016, **116**, 14120; (*b*) B. You, M. T. Tang, C. Tsai, F. Abild-Pedersen, X. Zheng and H. Li, *Adv. Mater.*, 2019, **31**, 1807001; (*c*) B. You, Y. Zhang, Y. Jiao, K. Davey and S. Z. Qiao, *Angew. Chem., Int. Ed.*, 2019, **58**, 11796.

3 (*a*) Z. W. She, J. Kibsgaard, C. F. Dickens, I. Chorkendorff, J. K. Nørskov and T. F. Jaramillo, *Science*, 2017, **355**, eaad4998; (*b*) B. You and Y. Sun, *ChemPlusChem*, 2016, **81**, 1045; (*c*) B. You, G. Han and Y. Sun, *Chem. Commun.*, 2018, **54**, 5943.

4 (*a*) D.-H. Nam, P. D. Luna, A. Rosas-Hernández, A. Thevenon, F. Li, T. Agapie, J. C. Peters, O. Shekhah, M. Eddaoudi and E. H. Sargent, *Nat. Mater.*, 2020, **19**, 266; (*b*) M. Jouny, G. S. Hutchings and F. Jiao, *Nat. Catal.*, 2019, **2**, 1062; (*c*) Y. Huang, A. D. Handoko, P. Hirunsit and B. S. Yeo, *ACS Catal.*, 2017, **7**, 1749.

5 (*a*) Y. Zheng, A. Vasileff, X. Zhou, Y. Jiao, M. Jaroniec and S. Z. Qiao, *J. Am. Chem. Soc.*, 2019, **141**, 7646; (*b*) Z. Sun, T. Ma, H. Tao and B. Han, *Chem*, 2017, **3**, 560; (*c*) D. D. Zhu, J. L. Liu and S. Z. Qiao, *Adv. Mater.*, 2016, **28**, 3423.

6 (*a*) W. Zhang, Y. Hu, L. Ma, G. Zhu, Y. Wang, X. Xue, R. Chen, S. Yang and Z. Jin, *Adv. Sci.*, 2018, **5**, 1700275; (*b*) T. K. Todorova, M. W. Schreiber and M. Fontecave, *ACS Catal.*, 2020, **10**, 1754; (*c*) L. Sun, V. Reddu, A. C. Fisher and X. Wang, *Energy Environ. Sci.*, 2020, **13**, 374.

7 (*a*) L. Wang, W. Chen, D. Zhang, Y. Du, R. Amal, S. Z. Qiao, J. Wu and Z. Yin, *Chem. Soc. Rev.*, 2019, **48**, 5310; (*b*) D. M. Weekes, D. A. Salvatore, A. Reyes, A. Huang and C. P. Berlinguette, *Acc. Chem. Res.*, 2018, **51**, 910; (*c*) J. Huang and R. Buonsanti, *Chem. Mater.*, 2019, **31**, 13.

8 (*a*) S. Nitopi, E. Bertheussen, S. B. Scott, X. Liu, A. K. Engstfeld, S. Horch, B. Seger, I. E. L. Stephens, K. Chan, C. Hahn, J. K. Nørskov, T. F. Jaramillo and I. Chorkendorff, *Chem. Rev.*, 2019, **119**, 7610; (*b*) A. Vasileff, C. Xu, Y. Jiao, Y. Zheng and S. Z. Qiao, *Chem*, 2018, **4**, 1809.

9 H. B. Yang, S.-F. Hung, S. Liu, K. Yuan, S. Miao, L. Zhang, X. Huang, H.-Y. Wang, W. Cai, R. Chen, J. Gao, X. Yang, W. Chen, Y. Huang, H. M. Chen, C. M. Li, T. Zhang and Bin Liu, *Nat. Energy*, 2018, **3**, 140.

10 (*a*) T. Zheng, K. Jiang, N. Ta, Y. Hu, J. Zeng, J. Liu and H. Wang, *Joule*, 2019, **3**, 265; (*b*) T. Zheng, K. Jiang and H. Wang, *Adv. Mater.*, 2018, **30**, 1802066; (*c*) J. Liu, X. Kong, L. Zheng, X. Guo, X. Liu and J. Shui, *ACS Nano*, 2020, **14**, 1093; (*d*) F. Yang, P. Song, X. Liu, B. Mei, W. Xing, Z. Jiang, L. Gu and W. Xu, *Angew. Chem., Int. Ed.*, 2018, **57**, 12303; (*e*) C. Zhao, X. Dai, T. Yao, W. Chen, X. Wang, J. Wang, J. Yang, S. Wei, Y. Wu and Y. Li, *J. Am. Chem. Soc.*, 2017, **139**, 8078; (*f*) X. Li, W. Bi, M. Chen, Y. Sun, H. Ju, W. Yan, J. Zhu, X. Wu, W. Chu, C. Wu and Y. Xie, *J. Am. Chem. Soc.*, 2017, **139**, 14889.

11 (*a*) Y. Chen, C. W. Li and M. W. Kanan, *J. Am. Chem. Soc.*, 2012, **134**, 19969; (*b*) B. A. Zhang, T. Ozel, J. S. Elias, C.

Costentin and D. G. Nocera, *ACS Cent. Sci.*, 2019, **5**, 1097; (*c*) Y. Yuan, L. Zhang, L. Li, H. Dong, S. Chen, W. Zhu, C. Hu, W. Deng, Z.-J. Zhao and J. Gong, *J. Am. Chem. Soc.*, 2019, **141**, 4791; (*d*) Y. Chen, Y. Huang, T. Cheng and W. A. Goddard, *J. Am. Chem. Soc.*, 2019, **141**, 11651; (*e*) D. Gao, Y. Zhang, Z. Zhou, F. Cai, X. Zhao, W. Huang, Y. Li, J. Zhu, P. Liu, F. Yang, G. Wang and X. Bao, *J. Am. Chem. Soc.*, 2017, **139**, 5652.

12 (*a*) S. Lin, C. S. Diercks, Y.-B. Zhang, N. Kornienko, E. M. Nichols, Y. Zhao, A. R. Paris, D. Kim, P. Yang, O. M. Yaghi and C. J. Chang, *Science*, 2015, **349**, 1208; (*b*) N. Kornienko, Y. Zhao, C. S. Kley, C. Zhu, D. Kim, S. Lin, C. J. Chang, O. M. Yaghi and P. Yang, *J. Am. Chem. Soc.*, 2015, **137**, 14129; (*c*) C. S. Diercks, S. Lin, N. Kornienko, E. A. Kapustin, E. M. Nichols, C. Zhu, Y. Zhao, C. J. Chang and O. M. Yaghi, *J. Am. Chem. Soc.*, 2018, **140**, 1116; (*d*) Z. Jiang, Y. Wang, X. Zhang, H. Zheng, X. Wang and Y. Liang, *Nano Res.*, 2019, **12**, 2330.

13 C.-T. Dinh, T. Burdyny, M. G. Kibria, A. Seifitokaldani, C. M. Gabardo, F. Pelayo García De Arquer, A. Kiani, J. P. Edwards, P. D. Luna, O. S. Bushuyev, C. Zou, R. Quintero-Bermudez, Y. Pang, D. Sinton and E. H. Sargent, *Science*, 2018, **360**, 783.

14 (*a*) X. Zheng, B. Zhang, P. D. Luna, Y. Liang, R. Comin, O. Voznyy, L. Han, F. Pelayo García De Arquer, M. Liu, C. T. Dinh, T. Regier, J. J. Dynes, S. He, H. L. Xin, H. Peng, D. Prendergast, X. Du and E. H. Sargent, *Nat. Chem.*, 2018, **10**, 149; (*b*) L. Q. Zhou, C. Ling, H. Zhou, X. Wang, J. Liao, G. K. Reddy, L. Deng, T. C. Peck, R. Zhang, M. S. Whittingham, C. Wang, C.-W. Chu, Y. Yao and H. Jia, *Nat. Commun.*, 2019, **10**, 4081.

15 J. Qiao, Y. Liu, F. Hong and J. Zhang, *Chem. Soc. Rev.*, 2014, **43**, 631.

16 D. Gao, R. M. Arán-Ais, H. S. Jeon and B. R. Cuenya, *Nat. Catal.*, 2019, **2**, 198.

17 M. B. Ross, P. D. Luna, Y. Li, C.-T. Dinh, D. Kim, P. Yang and E. H. Sargent, *Nat. Catal.*, 2019, **2**, 648.

18 D. Voiry, H. S. Shin, K. P. Loh and M. Chhowalla, *Nat. Rev. Chem.*, 2018, **2**, 0105.

19 R. M. Arán-Ais, D. Gao and B. R. Cuenya, *Acc. Chem. Res.*, 2018, **51**, 2906.

20 R.-B. Song, W. Zhu, J. Fu, Y. Chen, L. Liu, J.-R. Zhang, Y. Lin and J.-J. Zhu, *Adv. Mater.*, 2019, **31**, 1903796.

21 X. Wang, J. Ferreira de Araújo, W. Ju, A. Bagger, H. Schmies, S. Kühl, J. Rossmeisl and P. Strasser, *Nat. Nanotechnol.*, 2019, **14**, 1063.

22 E. Pérez-Gallent, M. C. Figueiredo, F. Calle-Vallejo and M. T. M. Koper, *Angew. Chem., Int. Ed.*, 2017, **56**, 3621.

23 M. C. Figueiredo, V. Trieu and M. T. M. Koper, *ACS Sustainable Chem. Eng.*, 2019, **7**, 10716.

24 X. Chang, A. Malkani, X. Yang and B. Xu, *J. Am. Chem. Soc.*, 2020, **142**, 2975.

25 M. Jouny, J.-J. Lv, T. Cheng, B. H. Ko, J.-J. Zhu, W. A. Goddard and F. Jiao, *Nat. Chem.*, 2019, **11**, 846.

26 T. Haas, R. Krause, R. Weber, M. Demler and G. Schmid, *Nat. Catal.*, 2018, **1**, 32.

27 D. Kim, C. S. Kley, Y. Li and P. Yang, *Proc. Natl. Acad. Sci. U. S. A.*, 2017, **114**, 10560.

28 T.-T. Zhuang, Y. Pang, Z.-Q. Liang, Z. Wang, L. Li, C.-S. Tan, J. Li, C. T. Dinh, P. D. Luna, P.-L. Hsieh, T. Burdyny, H.-H. Li, M. Liu, Y. Wang, F. Li, A. Proppe, A. Johnston, D.-H. Nam, Z.-Y. Wu, Y.-R. Zheng, A. H. Ip, H. Tan, L.-J. Chen, S.-H. Yu, S. O. Kelley, D. Sinton and E. H. Sargent, *Nat. Catal.*, 2018, **1**, 946.

29 J. Mock, Y. Zheng, A. P. Mueller, S. Ly, L. Tran, S. Segovia, S. Nagaraju, M. Köpke, P. Dürre and R. K. Thauer, *J. Bacteriol.*, 2015, **197**, 2965.

30 Gurudayal, D. Perone, S. Malani, Y. Lum, S. Haussener and J. W. Ager, *ACS Appl. Energy Mater.*, 2019, **2**, 4551.

31 B. You, Y. Zhang, P. Yin, D.-E. Jiang and Y. Sun, *Nano Energy*, 2018, **48**, 600.

32 T. Li, Y. Cao, J. He and C. P. Berlinguette, *ACS Cent. Sci.*, 2017, **3**, 778.

33 S. Verma, S. Lu and P. J. A. Kenis, *Nat. Energy*, 2019, **4**, 466.

34 Y. Li, X. Du, J. Huang, C. Wu, Y. Sun, G. Zou, C. Yang and J. Xiong, *Small*, 2019, **15**, 1901980.

35 B. Han, K. A. Stoerzinger, V. Tileli, A. D. Gamalski, E. A. Stach and Y. Shao-Horn, *Nat. Mater.*, 2017, **16**, 121.

36 B. M. Hunter, H. B. Gray and A. M. Müller, *Chem. Rev.*, 2016, **116**, 14120.

37 B. You, N. Jiang, X. Liu and Y. Sun, *Angew. Chem., Int. Ed.*, 2016, **55**, 9913.

38 B. You, X. Liu, N. Jiang and Y. Sun, *J. Am. Chem. Soc.*, 2016, **138**, 13639.

39 N. Jiang, B. You, R. Boonstra, I. M. T. Rodriguez and Y. Sun, *ACS Energy Lett.*, 2016, **1**, 386.

40 N. Jiang, X. Liu, J. Dong, B. You, X. Liu and Y. Sun, *ChemNanoMat*, 2017, **3**, 491.

41 B. You, X. Liu, X. Liu and Y. Sun, *ACS Catal.*, 2017, **7**, 4564.

42 V. S. K. Yadav and M. K. Purkait, *Energy Fuels*, 2016, **30**, 3340.

43 Y. Wang, A. Xu, Z. Wang, L. Huang, J. Li, F. Li, J. Wicks, M. Luo, D.-H. Nam, C.-S. Tan, Y. Ding, J. Wu, Y. Lum, C.-T. Dinh, D. Sinton, G. Zheng and E. H. Sargent, *J. Am. Chem. Soc.*, 2020, **142**, 5702.

44 (*a*) M. Luo and S. Guo, *Nat. Rev. Mater.*, 2017, **2**, 17059; (*b*) B. You, M. T. Tang, C. Tsai, F. Abild-Pedersen, X. Zheng and H. Li, *Adv. Mater.*, 2019, **31**, 1807001.

